Research Article

Superlow Power Consumption Artificial Synapses Based on WSe$_2$ Quantum Dots Memristor for Neuromorphic Computing

Zhongrong Wang,[1] Wei Wang,[1] Pan Liu,[1] Gongjie Liu,[1] Jiahang Li,[1] Jianhui Zhao,[1] Zhenyu Zhou,[1] Jingjuan Wang,[1] Yifei Pei,[1] Zhen Zhao,[1] Jiaxin Li,[1] Lei Wang,[1] Zixuan Jian,[1] Yichao Wang,[2] Jianxin Guo,[3] and Xiaobing Yan[1]

[1]*Key Laboratory of Brain-Like Neuromorphic Devices and Systems of Hebei Province, College of Electronic and Information Engineering, Hebei University, Baoding 071002, China*
[2]*Department of Clinical Laboratory Medicine, Taizhou Central Hospital (Taizhou University Hospital), Taizhou 318000, China*
[3]*College of Physics Science and Technology, Hebei University, Baoding 071002, China*

Correspondence should be addressed to Xiaobing Yan; yanxiaobing@ime.ac.cn

As the emerging member of zero-dimension transition metal dichalcogenide, WSe$_2$ quantum dots (QDs) have been applied to memristors and exhibited better resistance switching characteristics and miniaturization size. However, low power consumption and high reliability are still challenges for WSe$_2$ QDs-based memristors as synaptic devices. Here, we demonstrate a high-performance, superlow power consumption memristor device with the structure of Ag/WSe$_2$ QDs/ La$_{0.3}$Sr$_{0.7}$MnO$_3$/SrTiO$_3$. The device displays excellent resistive switching memory behavior with a R_{OFF}/R_{ON} ratio of $\sim 5 \times 10^3$, power consumption per switching as low as 0.16 nW, very low set, and reset voltage of ~ 0.52 V and$\sim$ -0.19 V with excellent cycling stability, good reproducibility, and decent data retention capability. The superlow power consumption characteristic of the device is further proved by the method of density functional theory calculation. In addition, the influence of pulse amplitude, duration, and interval was studied to gradually modulating the conductance of the device. The memristor has also been demonstrated to simulate different functions of artificial synapses, such as excitatory postsynaptic current, spike timing-dependent plasticity, long-term potentiation, long-term depression, and paired-pulse facilitation. Importantly, digit recognition ability based on the WSe$_2$ QDs device is evaluated through a three-layer artificial neural network, and the digit recognition accuracy after 40 times of training can reach up to 94.05%. This study paves a new way for the development of memristor devices with advanced significance for future low power neuromorphic computing.

1. Introduction

The human brain is a sophisticated and highly efficient information processing and storage system, including approximately 10^{11} neurons, and more than 10^{14} synapse connections [1–3]. The complicated neural network can process a large amount of information at the same time with a much lower power consumption of ~ 20 W [4, 5]. It performs better than traditional computers on complex tasks owing to the intrinsic characteristics of the integration of storage and computing, a key to overcoming the bottleneck of the von Neumann architecture [6–8]. However, there is

an urgent need for a basic unit with a simple structure to simulate biological synaptic activities to realize the intricate artificial neural network while reducing the huge demand for basic devices [3, 9–15]. Memristor, as one of the most promising technologies for constructing simulated neural networks for neuromorphic computing, has reconfigurable history-dependent resistance switching behavior and is competent to simulate the synaptic function of biological synapses [16, 17]. Although the great potential of the memristor in neuromorphic computing has been witnessed, its electrical characteristics, power consumption, linear conductance modulation, and other characteristics still need to be further

improved [18–20].

In recent years, transition metal dichalcogenides (TMDs) have received extensive attention owing to their excellent electronic, optical, and mechanical properties and extensive applications [21]. Among them, WSe_2 displays unique electrical and optical properties endowed by its high surface area and increased active edge sites urgently desired by plenty of practical applications [22, 23]. It has the advantages of high in-plane carrier mobility and electrostatic modulation of conductance and has been proven to be the first TMD material with bipolar transport characteristics, which opens up the opportunity for making high-performance nanoelectronic devices [24]. By transforming the 2D layered WSe_2 to zero dimension (WSe_2 quantum dots (QDs)) with a diameter of less than 10 nm, the quantum confinement and edge effects will cause additional electrical properties to be revealed [25, 26]. Due to the excellent features of WSe_2 QDs, and the unique features of QDs-based memory, such as simple sandwiched structure, fast operation, low power consumption, and low-cost fabrication, several researchers have applied WSe_2 QDs to the construction of memristors [21, 27]. For example, Perumalveeramalai et al. demonstrated a flexible memristor prepared by WSe_2 QDs sandwiched between two poly(methyl methacrylate) layers with a retention time of 7×10^3 s, switching endurance up to 100 cycles, desirable ON/OFF current ratio of 10^4 [23]. However, the application of WSe_2 QDs-based memristors in synaptic devices remains to be further investigated, and the realization and research of the synaptic plasticity in WSe_2 QDs memristors with low power consumption and high reliability will further equip the analogue neural networks for neuromorphic computing.

In this work, the resistive switching memristor with a novel device structure of Ag/WSe_2 QDs/$La_{0.3}Sr_{0.7}MnO_3$ (LSMO)/$SrTiO_3$ (STO) is presented, in which the Ag and WSe_2 QDs layer, LSMO layer, and STO layer were used as top electrode, active layer, bottom electrode, and buffer layer, respectively. According to the research results of Xu et al. [28], the LSMO bottom electrode has high self-resistance compared with traditional metal bottom electrodes, which can be used as a series resistor to provide compliance current; so, the device structure can be simplified. Meanwhile, the reset process can be implemented at low current, thereby reducing the energy consumption of the device. Fabricated WSe_2 QDs-based memristor device demonstrates excellent resistive switching characteristics with good data retention capability up to 1.5×10^4 s, switching endurance up to 100 cycles, desirable R_{OFF}/R_{ON} ratio of $\sim 5 \times 10^3$ with good cycling stability. Moreover, an ultra-low set voltage (V_{set}) of ~ 0.52 V, reset voltage (V_{reset}) of ~ -0.19 V, and power consumption per switching of 0.16 nW are achieved, which are much lower than that of other QDs-based memristors, as illustrated in Table S1 in the Supplementary Material. In addition, the superlow power consumption characteristic of the device is further demonstrated by density functional theory calculation. Furthermore, conduction regulation can be obtained by changing pulse amplitude, duration, and interval of the pulse sequences. According to the change of conductance representing synaptic weight, various synaptic functions such as excitatory postsynaptic current (EPSC), spike timing-dependent plasticity (STDP), long-term potentiation (LTP), long-term depression (LTD), and paired-pulse facilitation (PPF) are observed to simulate the biosynaptic behavior with proper rehearsal. More importantly, digit recognition ability based on the WSe_2 QDs device is verified according to a three-layer artificial neural network (ANN), and the digit recognition accuracy after 40 times of training can reach up to 94.05%. The fabricated Ag/WSe_2 QDs/LSMO/STO device could be further developed and applied for constructing neural network for future neuromorphic computing architecture.

2. Results

To observe the morphology of WSe_2 QDs, high-resolution transmission electron microscope (HR-TEM) image was acquired and shown in Figure 1(a). The dark spots in Figure 1(a) exhibit that WSe_2 QDs have clear boundaries and circular properties within a size range from 1.6 nm to 3.44 nm. The clearly visible lattice fringe spacing of the quantum dots is 0.23 nm, which is consistent with the literature [23]. In addition, the cross-sectional scanning electron microscope (SEM) image of the WSe_2 QDs/LSMO/STO device was achieved, as illustrated in Figure S1, which shows that the thickness of the WSe_2 QDs active layer is approximately 97 nm. Furthermore, to verify the successful deposition while identifying the chemical composition and states of LSMO bottom electrode and WSe_2 QDs active layer, the X-ray photoelectron spectroscopy (XPS) measurements were executed. The XPS detection results of main elements (C, O, La, Sr, Mn, O, Se, and W) of LSMO/STO and WSe_2 QDs/LSMO/STO were analyzed by CasaXPS (Version 2.3.13Dev29). Figure S2 in the Supplementary Material shows the XPS analysis result of the wide spectra and the core spectra of La 3d, Sr 3d, Mn 2p, and O 1 s of LSMO/STO, which clearly show the successfully formation of the LSMO bottom electrode film. The XPS wide spectra of WSe_2 QDs/LSMO/STO are exhibited in Figure S3 in the Supplementary Material. Figure 1(b) demonstrates the core spectra of W 4 f. The peaks located at 34.3 and 36.4 eV represent W $4f_{5/2}$ and W $4f_{7/2}$, respectively, proving the appearance of the oxidation state of W^{4+} on the surface of the WSe_2 QDs film [29, 30]. The peak located at 40.1 eV can be attributed to W $4f_{5/2}$ for W^{6+} (WO_3), which may be due to surface oxidation [31]. Figure 1(c) shows the core spectra of Se 3d. The peaks located at 54.0 and 54.9 eV represent Se $3d_{5/2}$ and Se $3d_{3/2}$, respectively [32]. Through the above XPS analysis of WSe_2 QDs/LSMO/STO, the presence of W and Se in WSe_2 QDs is clearly characterized. The calculated chemical stoichiometric ratio of W and Se is about 1 : 1.34, demonstrating that there are selenium vacancies in our prepared WSe_2 QDs film. Figure 1(d) depicts the current-voltage (I - V) curves over 100 cycles of the Ag/WSe_2 QDs/LSMO/STO device in the voltage sweep mode of $0 V \longrightarrow 1 V \longrightarrow 0 V \longrightarrow -0.5 V \longrightarrow 0 V$. The corresponding logarithmic form of I - V curves is illustrated in Figure 1(e). The device indicates typical bipolar resistance switching behavior, with the
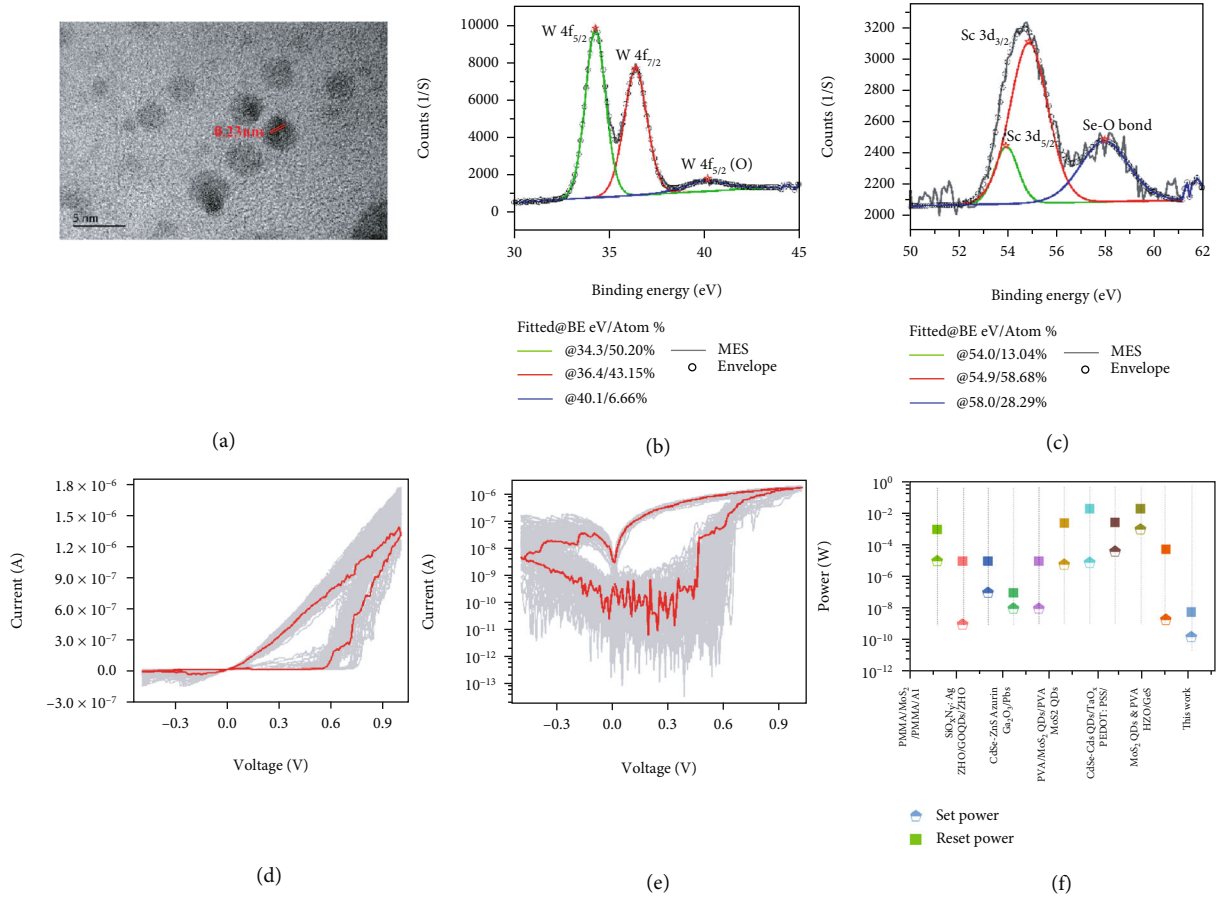
FIGURE 1: (a) HR-TEM image of WSe$_2$ QDs. (b) and (c) are XPS analysis results of WSe$_2$ QDs: (b) W 4f core spectra and (c) Se 3d core spectra. (d) I-V curves of Ag/WSe$_2$ QDs/LSMO/STO memristor clearly display resistive switching characteristics. (e) The logarithm form of (d). (f) Comparison of the power consumption of the device with the values of other QDs-based memristors.

transition of high-resistance state (HRS) and low-resistance state (LRS). As the positive scanning voltage increases and reaches $V_{set} \sim 0.52$ V, the memristor changes from HRS to LRS with a steeply incremental current from ~0.2 nA to 1 μA when applying a sweep voltage of 0 V ~ +1 V. During the reverse scanning from +1 V to -0.5 V, the memristor realizes the conversion from LRS to HRS under a V_{reset} of ~-0.19 V. It is interesting to note that the set and reset power consumption of the Ag/WSe$_2$ QDs/LSMO/STO device are as low as ~0.16 nW ($P_{set} = V_{set} \times I_{set}$) and ~6 nW ($P_{reset} = V_{reset} \times I_{reset}$), respectively, which are much lower than many reported QDs-based memristors [21, 33–41], as illustrated in Figure 1(f). Over 100 cycles of the I - V sweeps, the device displayed rather robust I - V curves and did not degrade, showing good endurance. In addition, a set of control experiments were conducted to verify the resistance switching behavior of WSe$_2$ QDs active layer. The I - V curves of the Ag/LSMO/STO device without spin-coated WSe$_2$ QDs layer (Figure S4 in the Supplementary Material) under the same experimental conditions show linear relationships of the voltage and current when the applied voltage is 1 ~ 5 V, which suggests that the WSe$_2$ QDs layer is the main reason for the resistance switching characteristics of Ag/WSe$_2$ QDs/LSMO/STO device.

To further study the uniformity of the device, the distribution of switching voltages of the device is analyzed and shown in Figures 2(a) and 2(b). The histogram statistics of the V_{set} and V_{reset} distributions over 100 cycles were performed by Gaussian fitting analysis (the black lines are the fitted curves). The V_{set} and V_{reset} of the device were confined in the range of 0.30 to 0.75 V and -0.15 to -0.49 V, respectively. The corresponding Gaussian fitted values of the V_{set} and V_{reset} were (0.52 ± 0.01) V and (-0.19 ± 0.05) V, respectively. The distribution of the switching voltages of the device was concentrated and less diffuse, which is conducive to the realization of accurately control and read of set and reset process, as well as the future practical application of Ag/WSe$_2$ QDs/LSMO/STO device. The low threshold voltage is very advantageous to reduce the power consumption of the memristor device. The distribution of HRS, LRS, and the R_{OFF}/R_{ON} ratios of the device is illustrated in Figures 2(c) and 2(d). The low and high resistance values are distributed on the order of 10^6 and 10^9, respectively. The device can maintain 10^2 switching cycles, indicating the excellent endurance ability, and the ratios of R_{OFF}/R_{ON} between the HRS and LRS can up to $\sim 5 \times 10^3$. Moreover, both HRS and LRS displayed long retentions of 10^4 s at the reading voltage of 0.5 V without being reduced, showing
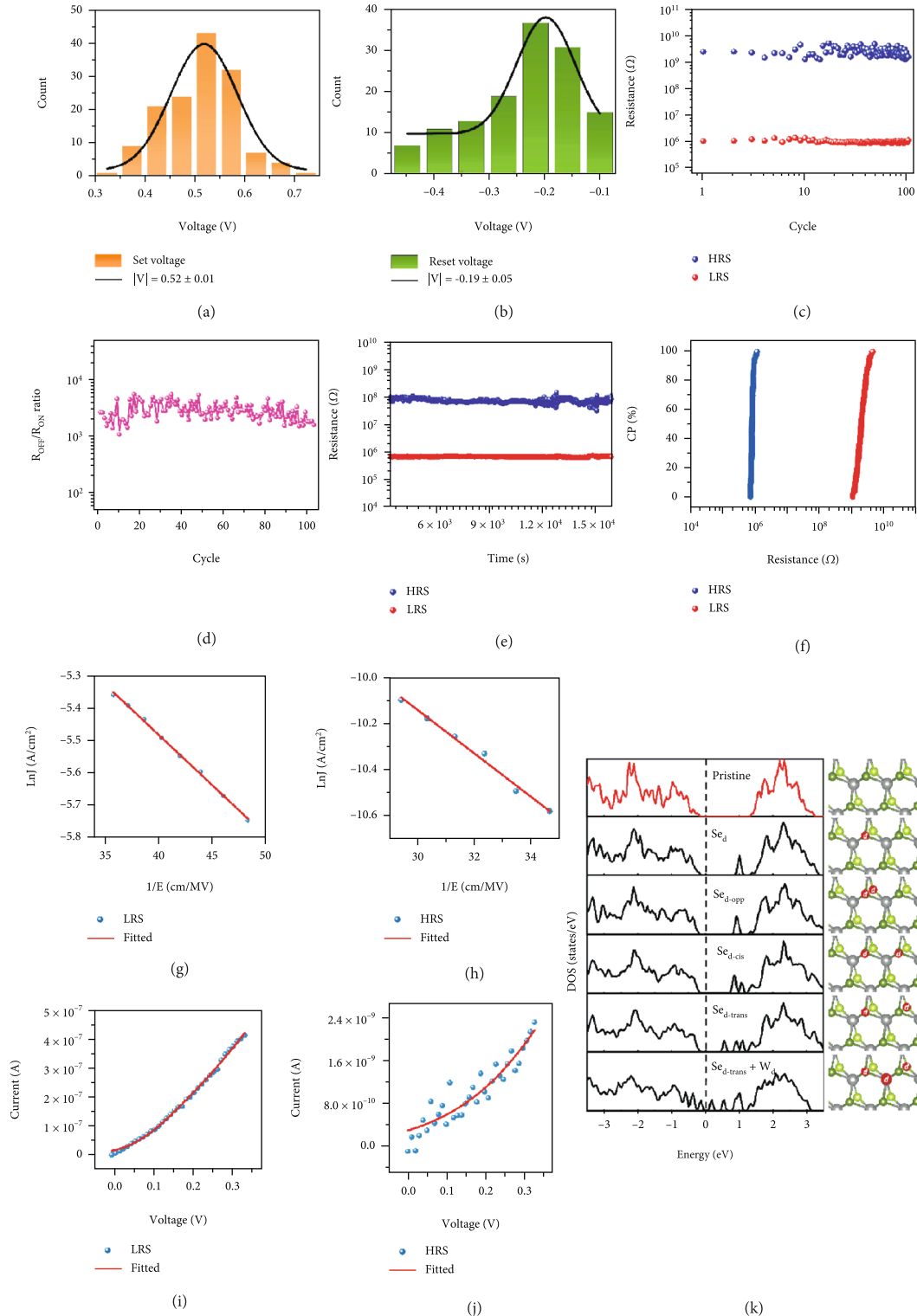
FIGURE 2: (a, b) Distribution histogram and Gaussian fitted curves of set and reset voltage. (c) Statistics of high and low resistance over 100 cycles. The read voltage is 0.2 V. (d) The ratios of R_{OFF}/R_{ON} of Ag/WSe$_2$ QDs/LSMO/STO device. (e) Retention data at HRS and LRS of the device in the room temperature. The read voltage is 0.5 V. (f) The cumulative probability plot of the HRS and LRS. (g) and (h) are the linear fitted curves of LRS and HRS by ln $(J) \propto 1/E$, demonstrating the trap-assisted tunneling (TAT) conduction mechanism. (i) and (j) are the fitted curves of LRS and HRS by formulas (1)–(3). (k) The density of states of pristine WSe$_2$ and the five defect models. The corresponding crystal structures are also shown. The dark green, light green, and gray balls represent upper layer Se atoms, lower layer Se atoms, and W atoms, respectively; "d" represents defect sites.

excellent stability (Figure 2(e)). The cumulative probability of HRS and LRS of the device is displayed in Figure 2(f), demonstrating the distinguishable HRS and LRS with the R_{OFF}/R_{ON} ratio of $\sim 5 \times 10^3$.

To further understand the conduction mechanism of Ag/WSe$_2$ QDs/LSMO/STO device, the switching characteristics were studied throughout the whole testing process. The analysis and fitting results are illustrated in Figures 2(g)–2(j). LRS and HRS of the I - V curves are fitted by the linear function $\ln (J) \propto 1/E$, respectively (Figures 2(g) and 2(h)), and the results indicate that the conductive characteristic of the device is in accordance with the TAT conduction mechanism [42]. HRS and LRS of the I - V curves can be fitted with formulas (1)–(3). Based on the conductance theory of TAT conduction mechanism, the tunneling current (I) can be expressed as [19, 43]

$$I = N \times q \times v \qquad (1)$$

Here, N represents the total number of the closest traps that conduce to the conduction, and the transition rate v can be expressed as

$$v = v_0 \times f \times P \qquad (2)$$

v_0 represents the frequency factor, and the Fermi-Dirac distribution of electrons in the electrode can be calculated as $f = 1/[1 + \exp (E_b - E_t + F \times d)/kT)]$. E_b represents the height of the barrier between the electrode and the conduction band, and k and T are Boltzmann constant and room temperature, respectively. The transmission probability P can be defined as

$$P = \exp \left\{ -\frac{4}{3\hbar qF} \sqrt{2m_c} \left[E_t^{3/2} - (E_t - F \times d)^{3/2} \right] \right\} \qquad (3)$$

$\hbar$ and q represent the reduced Planck's constant and electronic charge quantity, respectively. F, d, and E_t represent the electric field intensity, tunneling distance, and defect trap energy lower than the conduction band, respectively [44]. By fitting with formulas (1)–(3), two parameters can be received from the fitting results in Figures 2(i) and 2(j): the tunneling distance d and the trap energy E_t. Figures 2(i) and 2(j) exhibit the fitting results of the I - V curves obtained by adjusting d and E_t, where N is regarded as a constant [45]. From the fitting results of LRS (Figure 2(i)), E_t and d are 1.32 eV and 0.4 nm, respectively. In HRS (Figure 2(j)), E_t and d are slightly increased to 1.44 eV and 0.41 nm, respectively. The obtained results illustrate that HRS has deeper defect energy level traps and larger tunneling distances. In the TAT model, the movement of electrons is realized with the aid of defects [42]. Therefore, the lower trap energy E_t and distance d in LRS are beneficial to carrier transport.

The chemical stoichiometric ratio of W and Se obtained by XPS characterization indicates that there are enormous number of Se-site defects (Se$_d$) in our prepared WSe$_2$QDs films, which is consistent with the reports that chalcogen defects are generally supposed to be the most common

intrinsic defects in TMDs [46, 47]. Therefore, we investigated the defect formation energies and defect electronic structures of several defect models in WSe$_2$, including one Se$_d$ and the composite defects. For the composite defects, two Se$_d$, as well as two Se$_d$ containing one W-site defect (W_d), are considered, whereas the above composite defects with two Se$_d$ may be arranged in opposite (opp), cis, or trans configurations. The defect formation energies for one Se$_d$ and the composite defect models are listed in Table S2 in the Supplementary Material. Figure 2(f) illustrates the calculated density of states (DOS) diagrams of pristine WSe$_2$ and the five most preferred defect models, i.e., the structure with one Se$_d$, the opposite, cis, and trans configurations of two Se$_d$ (Se$_{d\text{-}opp}$, Se$_{d\text{-}cis}$, and Se$_{d\text{-}trans}$), and the trans configuration of two Se$_d$ containing one W-site defect (Se$_{d\text{-}trans}$ + W_d). The computational details are shown in the Supplementary Material. As shown in Figure 2(f), the electronic structure of the pristine WSe$_2$ shows a band gap of about 1.6 eV, which is consistent with the previous report [48]. The presence of a Se$_d$ and composite defects prefers to lead to the generation of defect states in the band gap of WSe$_2$. A single Se$_d$ can create a single defect state 0.28 eV below the conduction band. In addition, the case of the spatial configuration with 2Se$_d$ proves to be extremely meaningful. Unlike a single Se$_d$, the presence of a second Se$_d$ results in the change of defect states and band energy of the opposite configuration but creates new and different defect states for the trans configurations. However, due to the composite defects of two Se$_d$ and W_d in the trans configurations, the defect state system distributed throughout the whole band gap is generated. The above analysis proves that the defect states formed by one Se$_d$ and composite defects are at deep energy levels with localized characteristics; therefore, current leakage is not prone to occur, which further explains and demonstrates the superlow consumption characteristic of the Ag/WSe$_2$ QDs/LSMO/STO device [19].

Similar to biological synapses, the conductance of our WSe$_2$ QDs-based device can not only be modulated by the pulse amplitude and duration but also by the pulse interval, which proves the synaptic plasticity of our device. To further investigate the conductance modulation properties of Ag/WSe$_2$ QDs/LSMO/STO device, a series of positive pulse sequences were introduced to the device. The controllability of the conductance modulation was investigated by changing the amplitude, duration, and interval of the applied pulse. The conductance of the device was recorded instantly after the excitation was applied, and the serials of pulses were expressed by different colors. Figure 3(a) indicates that the conductance and the amplitude of the device are positively correlated under the condition of the same number of pulses; that is, the conductance increases with the increasing pulse amplitude (the pulse interval and duration are both fixed at 50 μs). Figure 3(b) indicates that the conductance increases with the increasing pulse duration (the pulse amplitude is 4 V, and the pulse interval is 50 μs). Figure 3(c) illustrates that the conductance and the pulse interval are negatively correlated; in other words, the
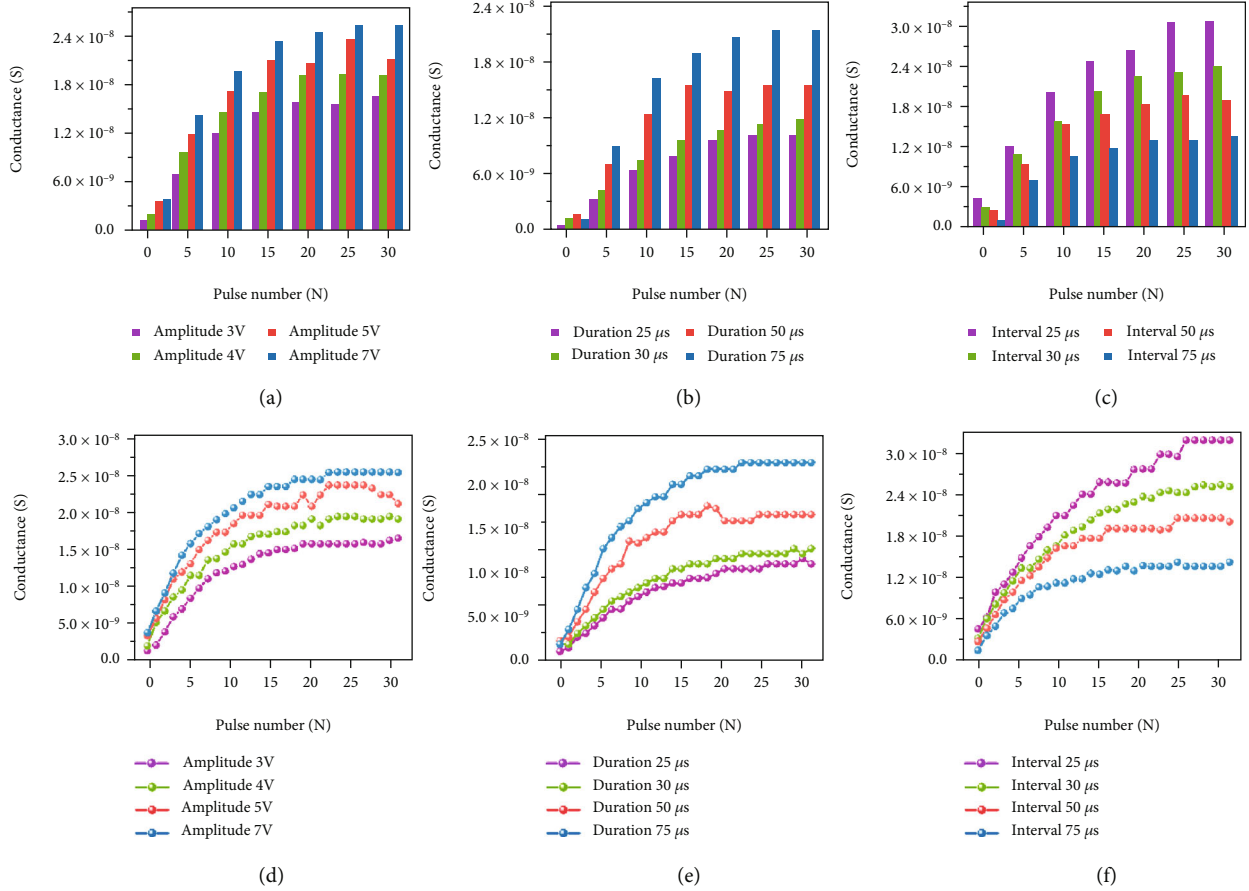
Figure 3: The conductance of the device for 30 pulse cycles was measured under different pulse (a) amplitudes, (b) durations, and (c) intervals. The device conductance was measured under a train of positive pulses: (d) the pulse duration and interval are both $50\,\mu s$ and different pulse amplitudes. (e) The pulse amplitude and interval are $4\,V$ and $50\,\mu s$, respectively, and different pulse durations. (f) The pulse amplitude and duration are $4\,V$ and $50\,\mu s$, respectively, and different pulse intervals.

conductance decreases with the increasing pulse interval (the pulse amplitude is $4\,V$, and the pulse duration is $50\,\mu s$). The effect of the pulse amplitude on the variation of the conductance is illustrated in Figure 3(d) under the constant pulse interval and duration (the pulse interval and duration are both fixed at $50\,\mu s$): a higher amplitude will result in an increased rate of rise in conductance and reach the saturated conductance value. The effect of the pulse duration on the variation of the conductance is illustrated in Figure 3(e) with a constant amplitude and interval (i.e., $4\,V$ and $50\,\mu s$). The results suggest that the rate of conductance increases as the pulse duration increases. The influence of the pulse interval on the variation of the conductance is shown in Figure 3(f) with a constant amplitude and duration (i.e., $4\,V$ and $50\,\mu s$), but the opposite result from Figure 3(e) is observed: the rate of conductance decreases with the increase of the pulse interval. In general, the conductance of the device can be finely modulated by the pulse number, amplitude, duration, and interval, which is conducive to the simulation of biological synaptic functions.

The forgetting curve of human memory is closely related to the approach of learning information. The "learning approach" (that is, the stimulus conditions) changes with the stimulation amplitude, duration, and interval [49]. EPSC means that the action signals and potentials of presynaptic neurons are transmitted to postsynaptic neurons through synapses under the action of an external excitation source. Figure 4 shows that when pulses of different numbers, amplitudes, durations, and intervals were applied to the device, the tail wave after the last pulse of each stimulation was measured and recorded [50]. After removing the applied square wave voltage, the synaptic weight would decay spontaneously in the absence of external inputs [51].

The correspondence between the forgetting behavior of the Ag/WSe$_2$ QDs/LSMO/STO device and the short-term plasticity (STP) of human neurons was investigated through an exponential decay equation describing the STP relaxation process:

$$M(t) = M_e + (M_0 - M_e)\exp\left(\frac{-t}{\tau}\right), \qquad (4)$$

where M_0 and M_e represent the initial and stable memory state, respectively, and τ represents the relaxation time constant. A larger τ value indicates a slower forgetting rate [50, 51].
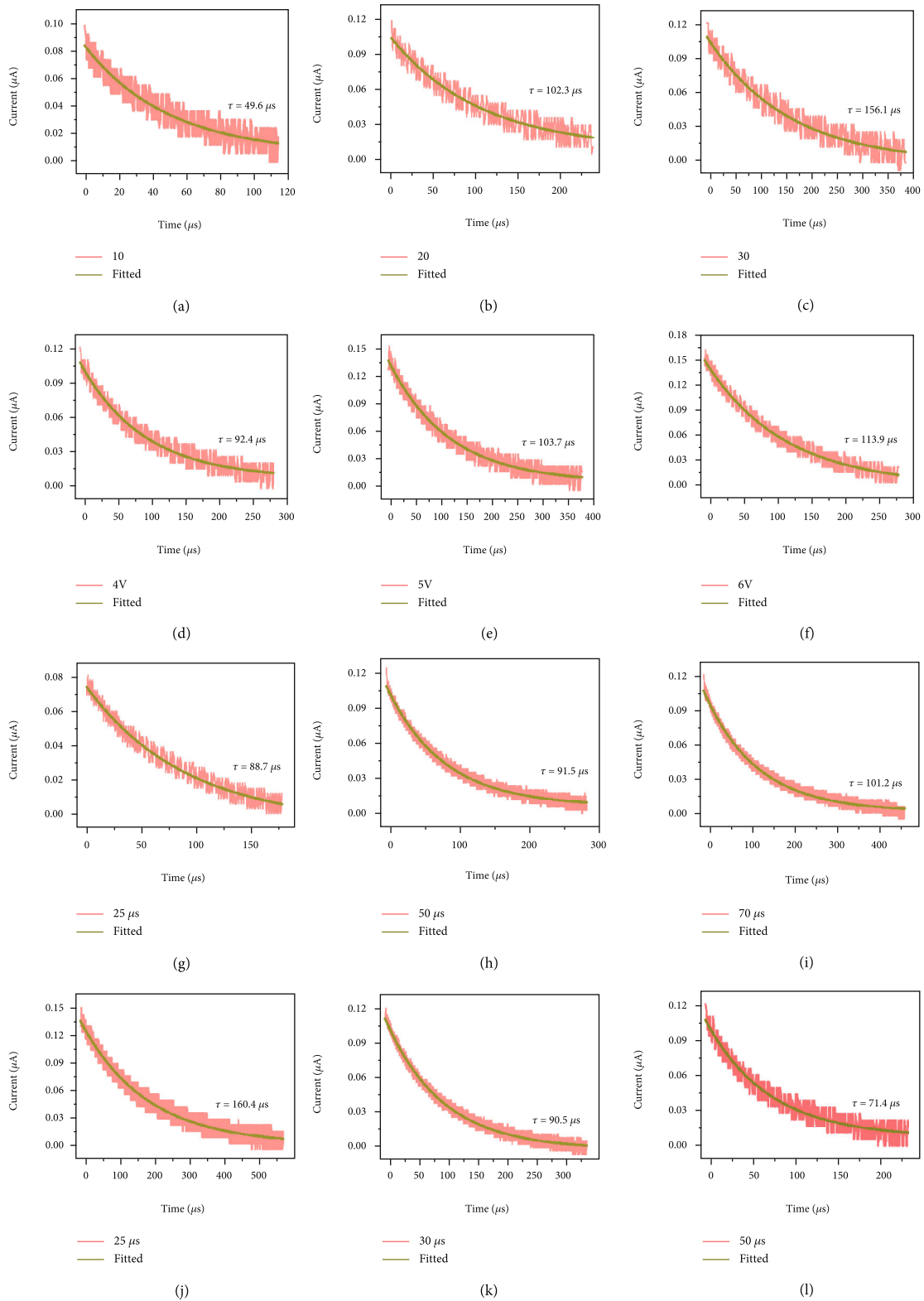
FIGURE 4: (a)–(c) Comparison of EPSC measurement response (orange curves) and fitted curves (green curves) under the condition of different pulse numbers. (d)–(f) Comparison of EPSC measurement response (orange curves) and fitted curves (green curves) under different square wave amplitudes. (g)–(i) Comparison of EPSC measurement response (orange curves) and fitted curves (green curves) under different pulse durations. (j)–(l) Comparison of EPSC measurement response (orange curves) and fitted curves (green curves) at different intervals.

Figures 4(a)–4(c) depict EPSC response results under different stimulation times. The fitted values of τ are 49.6 μs (Figure 4(a)), 102.3 μs (Figure 4(b)), and 156.1 μs (Figure 4(c)). If the applied number of pulses is larger, the stimulation time is longer, and the value of τ is larger, i.e., the forgetting is slower. Figures 4(d)–4(f) depict the response results corresponding to different amplitudes, where the fitted τ values are 92.4 μs (Figure 4(d)), 103.7 μs (Figure 4(e)), and 113.9 μs (Figure 4(f)). The results illustrate that the greater the amplitude, the greater the value of τ, i.e., the slower the forgetting. Figures 4(g)–4(i) show the response results of different durations, with different τ values of 88.7 μs (Figure 4(g)), 91.5 μs (Figure 4(h)), and 101.2 μs (Figure 4(i)). The results show that a larger pulse duration will result in a larger τ value, i.e., a slower forgetting rate. Figures 4(j)–4(l) are the response results with respect to different intervals, and the fitted τ values are 160.4 μs (Figure 4(j)), 90.5 μs (Figure 4(k)), and 71.4 μs (Figure 4(l)), respectively. The results show that a smaller interval will result in a larger τ value, i.e., a slower forgetting rate. The above analysis suggests that our device can realize EPSC simulation commendably.

STDP is one of the most significant biological features in the Hebbian learning rules for learning and memory, which can regulate the connection strength between human brain neurons [52, 53]. Figure 5(a) is a schematic illustration of a biological synapse, which is the connection between two neurons. The structure of Ag/WSe$_2$ QDs/LSMO/STO memristor device is similar to a typical nerve synapse. The top electrode (Ag) is considered as the presynaptic membrane, while the bottom electrode (LSMO) is considered as the postsynaptic membrane. Previous studies have demonstrated that metal ions such as Ag$^+$ and Cu^{2+} can migrate under the application of electric field and form conductive filaments, which is able to simulate the weight change of biological synapses caused by the release of Ca^{2+} or Na$^+$ from preneurons [3]. For devices based on Ag/WSe$_2$ QDs/LSMO/STO structure, the change of device resistance is studied when the driving voltage pulse sequence is applied. The setting mode of programming voltage is as below: the negative voltage pulse part is $-7\longrightarrow-0.2$ V, the voltage change step is -0.2 V; the positive voltage pulse part is $0.2\longrightarrow7$ V, and the voltage change step is 0.2 V. The duration and interval of each pulse are both 41.5 μs, and the obtained resistance change of the device is illustrated in Figure 5(b). In the negative voltage pulse part (blue), the absolute voltage value is increasing, and the resistance of the device increases with the decrease of negative voltage (depression). In the positive voltage pulse part (red), the absolute voltage value is increasing, and the resistance of the device decreases with the increase of positive voltage (potentiation). Therefore, the regulation of the weight of biological synapses (i.e., the variations of connection strength between biological synapses) can be simulated by the change of memristor resistance. STDP adjusts the synaptic weight by changing the interval from presynaptic to postsynaptic peaks (Δt). If the prestimulation time of the neuron is earlier than the poststimulation time of the neuron (i.e., $\Delta t > 0$), an increase in the postsynaptic current will caused. The phenomenon indicates that the stimulation signal of presynaptic neuron can be condu-

cive to promote the producing of postsynaptic neuron stimulation signal, and the synapse weight increases more as $|\Delta t|$ decreases. On the contrary, if the presynaptic stimulation time is later than the postsynaptic stimulation time (i.e., $\Delta t < 0$), the postsynaptic current will be inhibited. This indicates that the stimulation signal of presynaptic neurons plays an inhibitory role in the generation of postsynaptic neuron stimulation signals, and the synaptic weight decreases more as $|\Delta t|$ decreases. The STDP rule what we generally referred to occurs in the time window between excitement and excitement. When the action potential of presynaptic neurons is earlier than that of postsynaptic neurons, the weight of synaptic will increase, signifying LTP [34, 54–57]. On the contrary, when the action potential of presynaptic neurons is later than that of postsynaptic neurons, the weight of synaptic will decrease, signifying LTD [58]. This is called the anti-Hebbian learning rule. Following the above rules and definitions, we designed presynaptic and postsynaptic spike waveforms (as shown in Figure 5(c)) to stimulate Ag/WSe$_2$ QDs/LSMO/STO synapses, and the results (as shown in Figure 5(d)) demonstrate our device can implement this rule well. The fitted curve in Figure 5(d) is expressed by Equation (5):

$$\Delta W = Ae^{-\Delta t/\tau} + \Delta W_0 \qquad (5)$$

Here, A is the scale factor of the STDP function, τ is the time constant [59, 60], and W_0 is a constant which represents the nonassociative part of the synaptic change.

PPF is a typical physiological phenomenon in which the synaptic weight of biological synapses is increased in a short time during the continuous release of calcium ions at the presynaptic end owing to the presynaptic influx of ions. In a pair of presynaptic stimuli, when the second stimulus is triggered within a short time interval, the post-synaptic response of the second stimulus will be greater than that of the first stimulus, resulting in synaptic weights [61, 62]. In order to prove the PPF phenomenon in our device, a pulse with a pulse duration of 1.25 ms and a voltage amplitude of ±1 V was applied to Ag top electrodes. The correlation between synaptic weight and pulse time interval are shown in Figures 5(e) and 5(f). The pulse waveforms applied to the device for PPF simulation are illustrated in Figure S5 in the Supplementary Material. The ratios of PPF are expressed by [37]:

$$\text{PPF} = \frac{(G_2 - G_1)}{G_1} \times 100\% = C_1 \exp\left(\frac{-t}{\tau_1}\right) + C_2 \exp\left(\frac{-t}{\tau_2}\right) \tag{6}$$

Here, G_1 and G_2 are the conductance values after the action of the previous and subsequent pulses, respectively, and τ_1 and τ_2 are the fitted time constants, corresponding to the fast and slow decaying components, respectively [18]. For a positive voltage pulse, the fitted τ_1 and τ_2 are 48 μs and 700 μs, respectively (Figure 5(e)), while for a negative voltage pulse, the fitted τ_1 and τ_2 are 48 μs and 855 μs, respectively (Figure 5(f)). Our
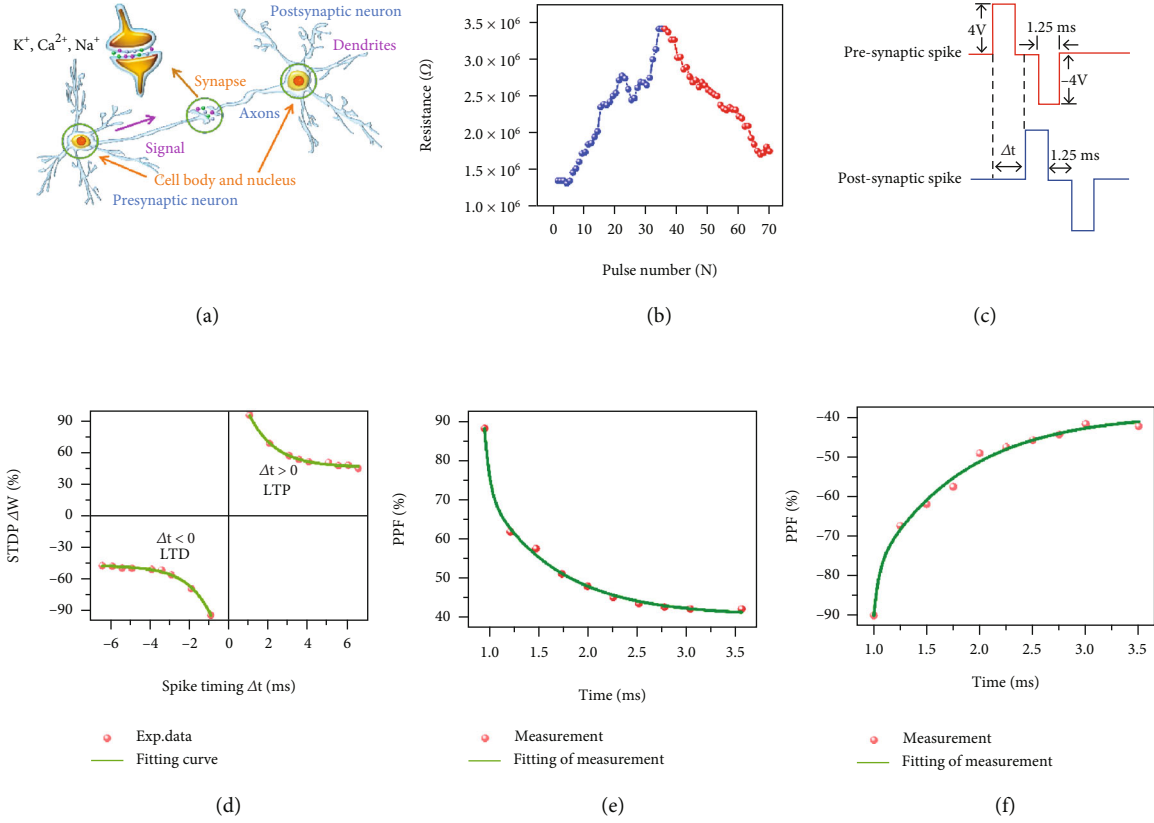
(a)

(b)

(c)

(d)

(e)

(f)

FIGURE 5: Simulation of the characteristics of STDP and PPF in biological synapses. (a) Schematic illustration of the structure of biological synapses. (b) The relationship between the pulse number and the resistance of the device. Applying a negative/positive pulse to the device will cause a decrease/increase in resistance, which represents the modulation of synaptic weight owing to enhancing or suppressing the pulses. (c) Schematic diagram of the pulse waveforms applied to the device for STDP simulation. (d) Measured STDP characteristics of Ag/WSe$_2$ QDs/LSMO/STO device, the green lines are the curves fitted by Equation (5). (e, f) Measured PPF characteristics of Ag/WSe$_2$ QDs/LSMO/STO device, (e) and (f) are the test results after applying positive and negative voltage pulses, respectively.

results indicate that as the pulse interval was decreased, the memory effect of the prespiking pulse on subsequent pulses was improved, which is excellently consistent with biological synapses.

To better evaluate the application of the Ag/WSe$_2$ QDs/LSMO/STO device in neuromorphic computing, we built a three-layer ANN to simulate the performance of the WSe$_2$ QDs-based memristor, including the input layer, hidden layer, and output layer in the network, as illustrated in Figure 6(a). Here, two datasets are used for evaluation, small images (8×8 pixels) of hand-written digits from the "Optical Recognition of Handwritten Digits" (ORHD) dataset [63] and large images (28×28 pixels) of hand-written digits from the "Modified National Institute of Standards and Technology" (MNIST) dataset [64], and the representative images of the MNIST dataset are illustrated in Figure 6(b). In the process of neural network simulation based on the WSe$_2$ QDs device, the weights between the neurons will be mapped to the intersection of the horizontal bar and the vertical bar in the crossbar based on the WSe$_2$ QDs device (Figure S6 in the Supplementary Material) [65]. A crossbar, considered part of the "neural core," is used to perform vector-matrix multiplication and outer product update operations (Figure S7 in the Supplementary Material). The detailed

simulation process is shown in the Supplementary Material. After 40 times of training in ANN, the recognition accuracy of WSe$_2$ QDs-based device in recognizing small images reaches 91.59%, and the ideal performance of floating-point-based neural networks [66] is 96.71%, which represents theoretical limit of the simulator, as illustrated in Figure 6(c). The recognition accuracy of WSe$_2$ QDs-based device reaches 94.05% in recognizing large images, and the ideal performance of the floating-point-based neural network reaches 98.19%, as illustrated in Figure 6(d). Compared to the work of Ge et al. [66], the image recognition accuracy of our devices for large images is improved by 3.05%. The above results fully demonstrate that the WSe$_2$ QDs-based device is very suitable for neuromorphic computing and provides new ideas for the further development of neuromorphic computing.

3. Discussion

In conclusion, we have presented a high-performance and superlow power consumption memristor device with the structure of Ag/WSe$_2$ QDs/LSMO/STO. The device exhibits excellent resistive switching characteristics with stable memory performance, with decent $R_{\text{OFF}}/R_{\text{ON}}$ ratio up to 5×10^3, superlow consumption of 0.16 nW, set and
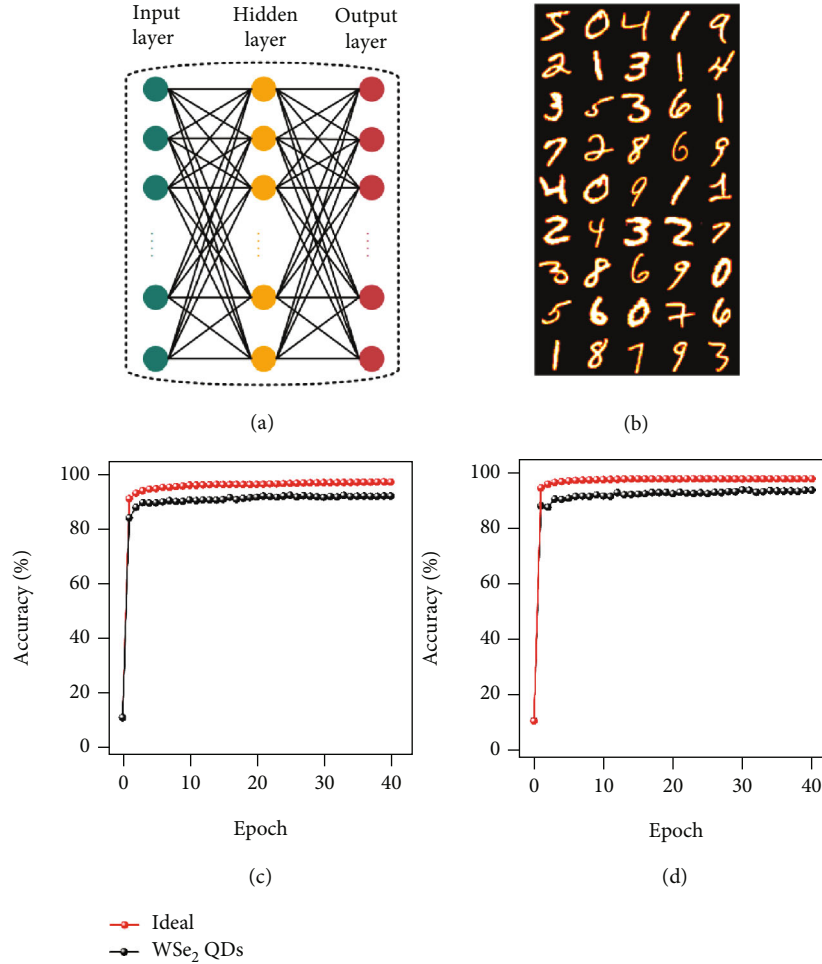
(a)

(b)

(c)

(d)

- Ideal
- WSe₂ QDs

FIGURE 6: Simulation of neural network based on WSe$_2$ QDs device. (a) A three-layer neural network structure is shown. It contains input layer, hidden layer and output layer. (b) Image representation of some handwritten digits in the MNIST dataset. (c) The comparison between the recognition accuracy of the optical recognition dataset of handwritten digits in the neural network simulation and the ideal case. After 40 training sessions, the ideal case recognition accuracy reaches 96.71%, and the device-based recognition accuracy reaches 91.59%. (d) Regarding the comparison of the recognition accuracy of the MNIST dataset in the neural network simulation with the ideal case, after 40 training sessions, the ideal case recognition accuracy reaches 98.19%, and the device-based recognition accuracy reaches 94.05%.

reset voltages as low as ~0.52 V and~ -0.19 V, and reliable repeatability. The movement of electrons assisted by defects obtained by the TAT model is responsible for the resistive switching behavior of the device. Meanwhile, density functional theory calculations demonstrate that the defect states formed by Se_d and W_d are at deep energy levels; so, current leakage does not easily occur, which further explain and prove the low power consumption characteristic of the device. Moreover, conduction regulation can be achieved by changing the external conditions, such as pulse amplitude, duration, and interval. And biological synaptic characteristics including EPSC, STDP, LTP, LTD, and PPF were successively proved. The recognition accuracy of digit images obtained by a three-layer ANN can reach up to 94.05%. This work demonstrates the Ag/ WSe$_2$ QDs/LSMO/STO memristor device holds great potential for application in low power consumption neuromorphic computing system.

4. Materials and Methods

4.1. Fabrication of the WSe$_2$ QDs Suspension. WSe$_2$ QDs were prepared based on the method reported in the reference [25]. First, WSe$_2$ powder was dispersed in N-methyl-2-pyrrolidone (NMP) to prepare a mortar with a concentration of 50 mg/mL. After dilution treatment in a glass vial containing 3 mL NMP and grinding for 30 min, the suspension was sonicated in an ice bath with a power of 260 W for 4 h. After regrinding for 30 minutes, the suspension was diluted to 15 mL and then resonication in an ice bath for another 4 h with a power of 260 W. After that, the resulting suspension was centrifuged at 8000 rpm for 20 minutes. After two cycles of centrifugation, the supernatant was collected and finally filtered with a 250 nm Teflon filter. In order to prevent WSe$_2$ from being oxidized, the entire ultrasonic treatment was carried out in a nitrogen atmosphere.

4.2. Fabrication of the Device. The sandwich structure device was fabricated by a combination of pulsed laser deposition (PLD), spin coating, and magnetron sputtering technology. First, the P-type Si substrate with a $1\,\mu$m-thick SiO_2 layer was cleaned with acetone, ethanol, and deionized water (DIW), respectively and then immersed in a mixture of hydrofluoric acid and DIW (1:3) to remove the silicon dioxide. Next, the STO buffer layer was deposited on the Si substrate by PLD under a growth temperature at 750°C, an oxygen pressure at 7.5 mTorr, and a laser repetition frequency of 5 Hz for 15 min. Then, the LSMO bottom electrode was deposited using a laser with an energy density of 350 mJ/cm^2 and repetition frequency of 2 Hz, while maintaining the growth temperature at 750°C and oxygen pressure at 200 mTorr for 30 min. Afterward, the WSe$_2$ QDs active layers were formed by spin-coating on the LSMO bottom electrode at a coating speed of 600 rpm for 60 s. Finally, an Ag top electrode film with a thickness of 60 nm and a diameter of 90 μm was fabricated by direct current magnetron sputtering technology under a pressure of 3 Pa and an Argon flow rate of 25 sccm.

4.3. Characterizations. HR-TEM (JEM-2100HR) was applied to identify the quality of the WSe$_2$ QDs. SEM (FEI Nova Nano SEM450) was utilized to identify the thickness of the WSe$_2$ QDs active layer. XPS (Thermo Fischer ESCALAB Xi+) was utilized to analyze the chemical configurations of the WSe$_2$ QDs using a 12.5 kV monochromatic Al Kα source. The C 1 s peak at 284.8 eV was used for charge calibration of all the binding energies. The electrical characterization experiments of Ag/WSe$_2$ QDs/LSMO/STO device, including the direct current I - V curves and pulse measurements, were determined at atmospheric pressure in air ambient using a Keithley 2400 digital source meter. A function/arbitrary waveform generator (RIGOL DG5102) was applied to conductance regulation experiment and tests EPSC, STDP, LTP, LTD, and PPF. An oscilloscope (RIGOL DS4022) was utilized to capture the waveforms throughout the pulse measurements. During all the electrical characterization experiments, the voltage bias was applied to the Ag electrode while the LSMO electrode and Si substrate were grounded all the time.

4.4. The Method Used in Digit Recognition Ability. The neural network simulations based on WSe$_2$ QDs memristors were performed in Python software. The Cross Sim simulator was used for supervised learning of the ORHD dataset and MNIST dataset. There are a total of 5620 8 × 8 pixel pictures of written digits in the ORHD dataset, of which 3823 are used for training and 1797 are used for testing. There are a total of 70,000 pictures of handwritten digits in the MNIST dataset, of which 60,000 are used for training and 10,000 are used for testing. During the simulations on both datasets, a learning rate of 0.1 was used.

Data Availability

All data needed to evaluate the conclusions in the paper are present in the paper and the Supplementary Material. Additional data related to this paper may be requested from the authors.

Conflicts of Interest

The authors declare that there is no conflict of interest regarding the publication of this article.

Authors' Contributions

X. Yan and Z. Wang conceived and designed the research. Z. Wang, W. Wang, J. H. Li, J. Zhao, and Z. Zhou conducted characterizations and electrochemical measurements. P. Liu performed density functional theory calculation. G. Liu performed the neural network simulation. J. Wang, Y. Pei, Z. Zhao, J. Li, L. Wang, Z. Jian, Y. Wang, and J. Guo added the experimental data. All authors discussed and analyzed the data. X. Yan, Z. Wang, and W. Wang cowrote the manuscript. All authors contributed to the general discussion. Zhongrong Wang and Wei Wang contributed equally to this work.

Acknowledgments

Supplementary Materials

Supplementary Materials Figures and figure captions: Figure S1: the cross-sectional SEM image of the WSe$_2$ QDs/LSMO/STO device. Figure S2: XPS analysis result of the LSMO/STO device. Figure S3: XPS wide spectra of the WSe$_2$ QDs/LSMO/STO device. Figure S4: the I - V curves of the Ag/LSMO/STO device without spin-coated WSe$_2$ QDs layer. Figure S5: schematic diagram of the pulse waveforms applied to the device for PPF simulation. Figure S6: the schematic diagram of the crossbar based on the WSe$_2$ QDs device. Figure S7: the neural core. Figure S8: schematic

diagram of digital image input. Tables and table captions: Table S1: key parameters compared with other QDs-based memristors. Table S2: the defect formation energies of defect configurations for WSe_2. Table S3: D/A and A/D attributes. *(Supplementary Materials)*

References

[1] H. Chen, C. Liu, Z. Wu et al., "Time-tailoring van der Waals heterostructures for human memory system programming," *Advanced Science*, vol. 6, no. 20, p. 1901072, 2019.

[2] J. Shen, B. Zhou, F. Wang et al., "Low consumption two-terminal artificial synapse based on transfer-free single-crystal MoS_2 memristor," *Nanotechnology*, vol. 31, no. 26, p. 265202, 2020.

[3] Y. Pei, Z. Zhou, A. P. Chen, J. Chen, and X. Yan, "A carbon-based memristor design for associative learning activities and neuromorphic computing," *Nanoscale*, vol. 12, no. 25, pp. 13531–13539, 2020.

[4] A. Thomas, "Memristor-based neural networks," *Journal of Physics D: Applied Physics*, vol. 46, no. 9, p. 093001, 2013.

[5] D. Kuzum, S. Yu, and H. P. Wong, "Synaptic electronics: materials, devices and applications," *Nanotechnology*, vol. 24, no. 38, p. 382001, 2013.

[6] G. Lee, J. H. Baek, F. Ren, S. J. Pearton, G. H. Lee, and J. Kim, "Artificial neuron and synapse devices based on 2D materials," *Small*, vol. 17, no. 20, p. 2100640, 2021.

[7] S. Wang, L. Liu, L. Gan et al., "Two-dimensional ferroelectric channel transistors integrating ultra-fast memory and neural computing," *Nature Communications*, vol. 12, no. 1, p. 53, 2021.

[8] A. Calimera, E. Macii, and M. Poncino, "The human brain project and neuromorphic computing," *Functional Neurology*, vol. 28, no. 3, pp. 191–196, 2013.

[9] J. Zhao, Z. Zhou, Y. Zhang et al., "An electronic synapse memristor device with conductance linearity using quantized conduction for neuroinspired computing," *Journal of Materials Chemistry C*, vol. 7, no. 5, pp. 1298–1306, 2019.

[10] I. Boybat, M. Le Gallo, S. R. Nandakumar et al., "Neuromorphic computing with multi-memristive synapses," *Nature Communications*, vol. 9, no. 1, pp. 1–12, 2018.

[11] N. K. Upadhyay, H. Jiang, Z. Wang, S. Asapu, Q. Xia, and J. Joshua Yang, "Emerging memory devices for neuromorphic computing," *Advanced Materials Technologies*, vol. 4, no. 4, p. 1800589, 2019.

[12] L. Bao, J. Zhu, Z. Yu et al., "Dual-gated MoS_2 neuristor for neuromorphic computing," *ACS Applied Materials & Interfaces*, vol. 11, no. 44, pp. 41482–41489, 2019.

[13] T. F. Schranghamer, A. Oberoi, and S. Das, "Graphene memristive synapses for high precision neuromorphic computing," *Nature Communications*, vol. 11, no. 1, pp. 1–11, 2020.

[14] E. Lee, J. Kim, S. Bhoyate, K. Cho, and W. Choi, "Realizing scalable two-dimensional MoS_2 Synaptic devices for neuromorphic computing," *Chemistry of Materials*, vol. 32, no. 24, pp. 10447–10455, 2020.

[15] S. Kim, K. Heo, S. Lee et al., "Ferroelectric polymer-based artificial synapse for neuromorphic computing," *Nanoscale Horizons*, vol. 6, no. 2, pp. 139–147, 2021.

[16] K. Liao, P. Lei, M. Tu et al., "Memristor based on inorganic and organic two-dimensional materials: mechanisms, performance, and synaptic applications," *ACS Applied Materials & Interfaces*, vol. 13, no. 28, pp. 32606–32623, 2021.

[17] J. Zhou, W. Li, Y. Chen et al., "A monochloro copper phthalocyanine memristor with high-temperature resilience for electronic synapse applications," *Advanced Materials*, vol. 33, no. 5, p. 2006201, 2021.

[18] K. Wang, L. Li, R. Zhao et al., "A pure $2H-MoS_2$ nanosheet-based memristor with low power consumption and linear multilevel storage for artificial synapse emulator," *Advanced Electronic Materials*, vol. 6, no. 3, p. 1901342, 2020.

[19] X. Yan, Q. Zhao, A. P. Chen et al., "Vacancy-induced synaptic behavior in 2D WS_2 nanosheet–based memristor for low-power neuromorphic computing," *Small*, vol. 15, no. 24, p. 1901423, 2019.

[20] J. J. Yang, M. D. Pickett, X. Li, D. A. A. Ohlberg, D. R. Stewart, and R. S. Williams, "Memristive switching mechanism for metal/oxide/metal nanodevices," *Nature Nanotechnology*, vol. 3, no. 7, pp. 429–433, 2008.

[21] S. Koduvayur Ganeshan, V. Selamneni, and P. Sahatiya, "Water dissolvable MoS_2 quantum dots/PVA film as an active material for destructible memristors," *New Journal of Chemistry*, vol. 44, no. 28, pp. 11941–11948, 2020.

[22] C. Tan, X. Cao, X. J. Wu et al., "Recent advances in ultrathin two-dimensional nanomaterials," *Chemical Reviews*, vol. 117, no. 9, pp. 6225–6331, 2017.

[23] C. Perumalveeramalai, F. Li, T. Guo, and T. W. Kim, "Flexible memristive device based on WSe_2 quantum dots sandwiched between two poly (methyl methacrylate) layers," *IEEE Electron Device Letters*, vol. 40, no. 7, pp. 1088–1091, 2019.

[24] P. C. Yeh, W. Jin, N. Zaki et al., "Layer-dependent electronic structure of an atomically heavy two-dimensional dichalcogenide," *Physical Review B*, vol. 91, no. 4, p. 041407, 2015.

[25] X. Zhang, Z. Lai, Z. Liu et al., "A facile and universal top-down method for preparation of monodisperse transition-metal dichalcogenide nanodots," *Angewandte Chemie International Edition*, vol. 54, no. 18, pp. 5425–5428, 2015.

[26] N. S. Arul and V. Nithya, "Molybdenum disulfide quantum dots: synthesis and applications," *RSC Advances*, vol. 6, no. 70, pp. 65670–65682, 2016.

[27] D. Wang, F. Ji, X. Chen, Y. Li, B. Ding, and Y. Zhang, "Quantum conductance in MoS_2 quantum dots-based nonvolatile resistive memory device," *Applied Physics Letters*, vol. 110, no. 9, p. 093501, 2017.

[28] Z. Xu, L. Yu, Y. Wu et al., "Low-energy resistive random access memory devices with no need for a compliance current," *Scientific Reports*, vol. 5, no. 1, p. 10409, 2015.

[29] L. Tao, F. Meng, S. Zhao et al., "Experimental and theoretical evidence for the ferromagnetic edge in WSe_2 nanosheets," *Nanoscale*, vol. 9, no. 15, pp. 4898–4906, 2017.

[30] S. Hussain, K. Akbar, D. Vikraman et al., "$WS_{(1-x)}Se_x$ nanoparticles decorated three-dimensional graphene on nickel foam: a robust and highly efficient electrocatalyst for the hydrogen evolution reaction," *Nanomaterials*, vol. 8, no. 11, p. 929, 2018.

[31] X. Xu, W. Xu, L. Zhang et al., "Interface engineering heterostructured MoS_2/WS_2-reduced graphene oxide for enhanced hydrogen evolution electrocatalysts," *Separation and Purification Technology*, vol. 278, p. 119569, 2021.

[32] S. Luo, K. Liao, P. Lei et al., "A synaptic memristor based on two-dimensional layered WSe_2 nanosheets with short- and long-term plasticity," *Nanoscale*, vol. 13, no. 13, pp. 6654–6660, 2021.

[33] S. T. Han, Y. Zhou, B. Chen et al., "Hybrid flexible resistive random access memory-gated transistor for novel nonvolatile data storage," *Small*, vol. 12, no. 3, pp. 390–396, 2016.

[34] Z. Wang, S. Joshi, S. E. Savel'ev et al., "Memristors with diffusive dynamics as synaptic emulators for neuromorphic computing," *Nature Materials*, vol. 16, no. 1, pp. 101–108, 2017.

[35] X. Yan, L. Zhang, Y. Yang et al., "Highly improved performance in $Zr_{0.5}Hf_{0.5}O_2$ films inserted with graphene oxide quantum dots layer for resistive switching non-volatile memory," *Journal of Materials Chemistry C*, vol. 5, no. 42, pp. 11046–11052, 2017.

[36] A. K. Yagati, S. U. Kim, T. Lee, J. Min, and J. W. Choi, "Recombinant azurin-CdSe/ZnS hybrid structures for nanoscale resistive random access memory device," *Biosensors and Bioelectronics*, vol. 90, pp. 23–30, 2017.

[37] X. Yan, Y. Pei, H. Chen et al., "Self-Assembled Networked PbS Distribution Quantum Dots for Resistive Switching and Artificial Synapse Performance Boost of Memristors," *Advanced Materials*, vol. 31, no. 7, p. 1805284, 2019.

[38] A. Thomas, A. Resmi, A. Ganguly, and K. Jinesh, "Programmable electronic synapse and nonvolatile resistive switches using MoS_2 quantum dots," *Scientific Reports*, vol. 10, no. 1, pp. 1–10, 2020.

[39] J. Guo, S. Guo, X. Su et al., "Nonvolatile resistive switching memory device employing CdSe/CdS core/shell quantum dots as an electrode modification layer," *ACS Applied Electronic Materials*, vol. 2, no. 3, pp. 827–837, 2020.

[40] M. Chen, G. Dong, X. Li et al., "Influence of MoS_2 quantum dots size on the properties of memristor devices," *Optik*, vol. 207, p. 163776, 2020.

[41] Z. Zhu, Y. Pei, C. Gao, H. Wang, and X. Yan, "A Cu/HZO/GeS/Pt memristor for neuroinspired computing," *Physica Status Solidi-Rapid Research Letters*, vol. 15, no. 10, p. 2100072, 2021.

[42] M. P. Houng, Y. H. Wang, and W. J. Chang, "Current transport mechanism in trapped oxides: a generalized trap-assisted tunneling model," *Journal of Applied Physics*, vol. 86, no. 3, pp. 1488–1491, 1999.

[43] X. Yan, Z. Zhou, B. Ding, J. Zhao, and Y. Zhang, "Superior resistive switching memory and biological synapse properties based on a simple $TiN/SiO_2/p$-Si tunneling junction structure," *Journal of Materials Chemistry C*, vol. 5, no. 9, pp. 2259–2267, 2017.

[44] H. Y. Jeong, Y. Jin, S. J. Yun et al., "Heterogeneous defect domains in single-crystalline hexagonal WS_2," *Advanced Materials*, vol. 29, no. 15, p. 1605043, 2017.

[45] X. Yan, K. Wang, J. Zhao et al., "A new memristor with 2D $Ti_3C_2T_x$ MXene flakes as an artificial bio-synapse," *Small*, vol. 15, no. 25, p. 1900107, 2019.

[46] S. Zhang, C. G. Wang, M. Y. Li et al., "Defect structure of localized excitons in a WSe_2 monolayer," *Physical Review Letters*, vol. 119, no. 4, p. 046101, 2017.

[47] M. J. Shearer, W. Li, J. G. Foster, M. J. Stolt, R. J. Hamers, and S. Jin, "Removing defects in WSe_2 via surface oxidation and etching to improve solar conversion performance," *ACS Energy Letters*, vol. 4, no. 1, pp. 102–109, 2019.

[48] C. H. Chang, X. Fan, S. H. Lin, and J. L. Kuo, "Orbital analysis of electronic structure and phonon dispersion in MoS_2, $MoSe_2$, WS_2, and WSe_2 monolayers under strain," *Physical Review B*, vol. 88, no. 19, p. 195420, 2013.

[49] T. Ohno, T. Hasegawa, T. Tsuruoka, K. Terabe, J. K. Gimzewski, and M. Aono, "Short-term plasticity and long-term potentiation mimicked in single inorganic synapses," *Nature Materials*, vol. 10, no. 8, pp. 591–595, 2011.

[50] T. Chang, S. H. Jo, and W. Lu, "Short-term memory to long-term memory transition in a nanoscale memristor," *ACS Nano*, vol. 5, no. 9, pp. 7669–7676, 2011.

[51] Z. Q. Wang, H. Y. Xu, X. H. Li, H. Yu, Y. C. Liu, and X. J. Zhu, "Synaptic learning and memory functions achieved using oxygen ion migration/diffusion in an amorphous InGaZnO memristor," *Advanced Functional Materials*, vol. 22, no. 13, pp. 2759–2765, 2012.

[52] R. S. Zucker and W. G. Regehr, "Short-term synaptic plasticity," *Annual Review of Physiology*, vol. 64, no. 1, pp. 355–405, 2002.

[53] J. H. Ryu, C. Mahata, and S. Kim, "Long-term and short-term plasticity of Ta_2O_5/HfO_2 memristor for hardware neuromorphic application," *Journal of Alloys and Compounds*, vol. 850, p. 156675, 2021.

[54] L. F. Abbott and S. B. Nelson, "Synaptic plasticity: taming the beast," *Nature Neuroscience*, vol. 3, no. 11, pp. 1178–1183, 2000.

[55] P. D. Roberts and C. C. Bell, "Spike timing dependent synaptic plasticity in biological systems," *Biological Cybernetics*, vol. 87, no. 5-6, pp. 392–403, 2002.

[56] Y. Li, Y. Zhong, L. Xu et al., "Ultrafast synaptic events in a chalcogenide memristor," *Scientific Reports*, vol. 3, no. 1, pp. 1–7, 2013.

[57] M. F. Bear and R. C. Malenka, "Synaptic plasticity: LTP and LTD," *Current Opinion in Neurobiology*, vol. 4, no. 3, pp. 389–399, 1994.

[58] X. Yan, J. Zhao, S. Liu et al., "Memristor with Ag-cluster-doped TiO_2 films as artificial synapse for neuroinspired computing," *Advanced Functional Materials*, vol. 28, no. 1, p. 1705320, 2018.

[59] Y. Shi, K. Saito, H. Ishikuro, and T. Hiramoto, "Effects of traps on charge storage characteristics in metal-oxide-semiconductor memory structures based on silicon nanocrystals," *Journal of Applied Physics*, vol. 84, no. 4, pp. 2358–2360, 1998.

[60] T. Ishii, T. Osabe, T. Mine, T. Sano, B. Atwood, and K. Yano, "A poly-silicon TFT with a sub-5-nm thick channel for low-power gain cell memory in mobile applications," *IEEE Transactions on Electron Devices*, vol. 51, no. 11, pp. 1805–1810, 2004.

[61] G. Dastgeer, H. Abbas, D. Y. Kim, J. Eom, and C. Choi, "Synaptic characteristics of an ultrathin hexagonal boron nitride (h-BN) diffusive memristor," *Physica Status Solidi-Rapid Research Letters*, vol. 15, no. 1, p. 2000473, 2020.

[62] H. Abbas, Y. Abbas, G. Hassan et al., "The coexistence of threshold and memory switching characteristics of ALD HfO_2 memristor synaptic arrays for energy-efficient neuromorphic computing," *Nanoscale*, vol. 12, no. 26, pp. 14120–14134, 2020.

[63] K. Bache and M. Lichman, "UCI Machine Learning Repository," 2017, https://archive.ics.uci.edu/ml/index.php/.

[64] Y. L. Cun, C. Cortes, and C. J. Burges, "The MNIST Database of Handwritten Digits," 2016, http://yann.lecun.com/exdb/mnist/.

[65] J. Rao, Z. Fan, L. Hong et al., "An electroforming-free, analog interface-type memristor based on a $SrFeO_x$ epitaxial heterojunction for neuromorphic computing," *Materials Today Physics*, vol. 18, p. 100392, 2021.

[66] C. Ge, G. Li, Q. L. Zhou et al., "Gating-induced reversible H_xVO_2 phase transformations for neuromorphic computing," *Nano Energy*, vol. 67, p. 104268, 2020.